Chapter One

Introduction

1.1 Overview

For many materials, changes in internal properties are accompanied by large changes of shape (strictions). Three important classes include ferroelastic, ferroelectric, and ferromagnetic materials [1], [2]. Their structural properties couple strongly to the alignment of mechanical, electric, and magnetic dipoles, respectively. Precisely the same symmetry principles are thought to apply to each class of strictive materials, so that elucidation of one finds immediately application to others.

For materials with large strictions, this coupling is well-suited for study using thin films. Single crystal epilayers can be synthesized with chosen epitaxial constraints such as strain and clamping. Together these can strongly modify internal polarization and phase relationships. The enhanced opportunities for materials physics which thin films provide have long been recognized. Prior to the development of molecular beam epitaxy (MBE), early synthesis efforts were less effective and sample composition was used as a principal control variable. For example, early research on amorphous transition metal-rare earth (TM-RE) alloys showed that these systems exhibit properties such as magnetic anisotropy which could be tailored by growth conditions or by composition [3],[4]. Subsequent investigations with higher-quality single-crystal specimens, facilitated by advances in thin film synthesis, permitted identification of specific terms in the magnetic Hamiltonian for these systems. Individual terms could be controlled and studied by epitaxy [5]. The state of the art in this field was evidenced in a recent study by Huth and co-workers who used knowledge of the magnetic Hamiltonian for the Laves phase compound $TbFe_2$ to synthesize thin films with perpendicular magnetic anisotropy, which is otherwise energetically unfavorable, by creating the necessary state of epitaxial strain [6].

The strictive properties of materials can be explored in thin films by the effects of composition, strain, clamping, and interface quality. The present research focuses on the role of strain in breaking the symmetry and coupling to the strictive properties of the rare earth metals. The utility of strain as a control variable has been recognized for ferroelastic [7], ferroelectric [8], and ferromagnetic [9] systems, but it may require developing new synthesis pathways. Studies of the way in which strain affects epitaxial magnetism are still in their infancy.

Previous Rare Earth Research

The rare earth metals have the largest known magnetostrictions, so that their magnetic and structural properties are strongly coupled. In 1986 Kwo and co-workers synthesized the first single-crystal rare earth thin films using Gd/Y grown by MBE [10]. It was quickly realized that the ability to tailor specimens precisely using MBE could create conditions in which specific magnetic interactions could be probed. Subsequent discoveries included the propagation of coherent helimagnetic order across non-magnetic spacer layers, and the role of two distinct magnetoelastic effects. These are: *strain*, which alters the magnetic behavior of heteroepitaxial thin films whose lattice parameters are strained from their bulk values (for example, T_C can be enhanced or surpressed by compressive or tensile stress); and *clamping*, in which epitaxy on a substrate strains the in-plane dimension and thereby alters the response of a magnetic material. An example occurs in the magnetism of strain-free Er grown in registry with a Y-Lu alloy, for which ferromagnetism is suppressed in the thin film. The magnetic properties can then be very different from the bulk properties, because the substrate eliminates the in-plane magnetostrictive lattice distortion [11][12]. The work in this thesis concerns the effects of strain on the ordering and phase diagram of Dy.

Since 1986 most research on rare earth thin films has concerned the materials properties of rare earth thin films grown with the hcp c-axis normal to the film plane. Such films proved relatively easy to synthesize, although the routine production of exceptional quality specimens with mosaicities below 0.1° has only recently been achieved [13]. This is due to the stability of the substrates, buffer layers, and rare earths used for these specimens, as discussed in more detail in Chapter 3.

Techniques for the routine synthesis of rare earths in other crystal orientations have been lacking with two notable exceptions. In 1988, Tsui and co-workers used polished, single-crystal Y substrates to synthesize single-crystal rare earths with the hcp a-axis and b-axis normal to the growth plane [9]. These were used to measure the anisotropy of the exchange coupling mechanism, which is a long-range effect directed mainly along the c-axis. Helimagnetic order in superlattices can be propagated through thick, non-magnetic spacer layers along the c-axis, but not along the a- or b-axes [14].

In 1994, Theis-Bröhl and co-workers examined the magnetic properties of “tilted” single-crystal Dy/Y superlattices [15],[16]. As first observed by Du [17], rare earths nucleate on Ta(211) with a high-index direction normal to the surface (the surface normal lies between the hcp $(1\bar{1}02)$ and $(1\bar{1}03)$ directions). Interestingly, the surfaces of these samples develop $(1\bar{1}02)$ and $(1\bar{1}05)$ facets; on each facet a coherent superlattice can be grown. Preliminary evidence suggests Dy in this orientation exhibits a superposition of magnetic properties deriving from different epitaxial constraints imposed separately upon the different facets.

An important part of the present work is the development of a reproducible technique whereby high-quality single-crystal thin films of rare earths can be grown on sapphire with the hcp b-axis normal to the growth plane. It turns out that the growth procedure is significantly more complicated than that required for c-axis rare earths, with five buffer layers required, not just one.

Research with the resulting b-axis-oriented samples holds great promise. While c-axis-oriented samples can be used to study a wide variety of magnetic properties, with epitaxial strain and clamping as control parameters, in c-axis samples the hexagonal symmetry of the basal plane is always preserved. b-axis-oriented samples, grown on appropriate buffer layers, offer the opportunity to selectively break the basal plane symmetry and to explore the resulting magnetic behavior. Specifically, the rare earths exhibit elegant and complex states of magnetic order which are sensitive to magnetocrystalline and shape anisotropy, and which can be strongly modified in b-axis-oriented samples.

Using the the successful procedure for b-axis rare earths, further research presented in this thesis has been able to probe the way magnetic properties change when the symmetry of the basal plane is broken. A preliminary study of symmetry reduction in Dy has been undertaken, and unexpected behavior has been observed. The results include strong modification of the transition between antiferromagnetic (AF) and ferromagnetic (FM) states, observation of strain-dependent easy magnetization axes, and dependence of magnetic ordering on the applied field. These results for Dy promise an exciting future for work with other b-axis-oriented rare earths.

The Thesis is organized in the following way. Chapter 1 introduces relevant background material about rare earth metals. Magnetic behavior is described together with specific terms in the Hamiltonian. Chapter 2 provides an overview of the experimental arrangements necessary for sample synthesis and for structural and magnetic measurements. Chapter 3 explains the growth procedure developed for the synthesis of b-axis-oriented rare earth metals. A complete description of the observed magnetic properties of b-axis-oriented Dy is given in Chapter 4, and interpretation and discussion of those properties is presented in Chapter 5. Two simple models of magnetic ordering were developed to provide a qualitative understanding of features observed in measurements of magnetic hysteresis. The dependence of the hysteresis loop shape on anisotropy, and the effect of domain wall pinning on coercivity are presented in Chapter 6.

The remainder of this Chapter provides background on the magnetic interactions and Dy which form the substance of this thesis. Beginning with a review of the rare earths metals, it describes the terms in the Hamiltonian which determine the magnetic properties.

Following a review of symmetry principles, the main interaction terms are described. The relevant magnetoelastic properties of Dy are then reviewed with emphasis on two aspects which are important to Chapter 5, the AF-FM phase transition and coercive fields. Finally, time-dependent magnetic phenomena are introduced, in connection with magnetic relaxation phenomena reported in Chapter 4.

1.2 Local Moments and Rare Earth Magnetism

The rare earths form the lanthanide series of metals from Ce to Lu in the Periodic Table. Most possess a trivalent outer shell configuration and highly-localized 4f inner shells. The localized and anisotropic nature of the 4f electrons, and their arrangement in a (usually) hexagonal unit cell, gives rise to the rich variety of magnetic, elastic, crystal field, and Fermi surface properties exhibited by the rare earths. Paramagnetic-to-antiferromagnetic (PM-AF) phase transitions occur at Néel temperatures, T_N; antiferromagnetic-to-ferromagnetic (AF-FM) phase transitions occur at a Curie temperatures, T_C. The latter is generally accompanied by a spontaneous magnetoelastically-driven lattice distortion or striction of the lattice which can amount to a factor of 1%. In the AF regime these materials exhibit a rich diversity of complex helimagnetic structures characterized by magnetization waves with periods of about 10 atomic planes. Some are used as examples in Figure 1.1.

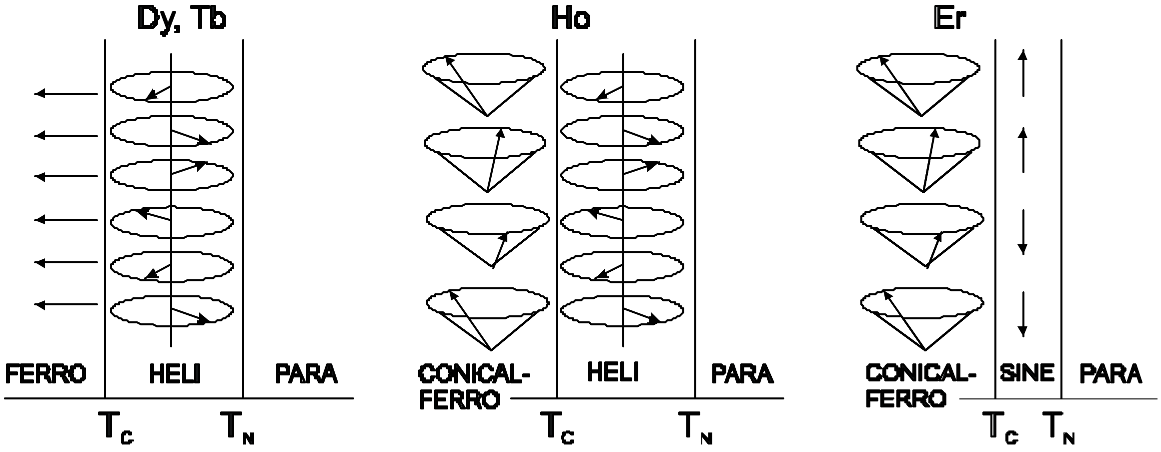

Figure 1.1. The spin structures in some of the rare earths at different temperatures.

While complicated, the magnetic behavior of rare earth metals is nevertheless described surprisingly well by models in which a lattice of atomic 4f shells exist in a uniform sea of conduction electrons [18]. The complete Hamiltonian for this “standard model” of local-moment magnetism contains over one dozen separate interactions, whose relative importance depends not only on its overall strength, but also on its relative contribution to a specific measurement or property [19].

The research in this thesis mainly concerns magnetostriction and the AF-FM phase transition. For this purpose the relevant magnetic free energy is described by the Hamiltonian,

$$H = H_{EL} + H_{EX} + H_{CF} + H_{ME} + H_S + H_Z\,. \tag{1.1}$$

The terms represent the elastic, exchange-coupling, crystal field, magnetoelastic, shape anisotropy, and Zeeman terms, respectively. These specific interactions are described in the following Sections.

Although mechanisms that change the spin-orbit interaction H_{SO} are not involved in this thesis, it is noteworthy for completeness that this final term plays an important role by establishing the strength of H_{CF} for the rare earths metals. Electrostatic interactions within a crystal generally couple directly only to charges. For the rare earths, however, the strong spin-orbit interaction ensures the magnetic spins are also coupled to specific crystallographic directions, and therefore H_{CF} is an important term [20],[21].

1.3 Terms in the Magnetoelastic Hamiltonian

This Section describes the separate terms in the magnetoelastic Hamiltonian. Symmetry and irreducible representations are first introduced, to establish the general formalism subsequently employed to describe the elastic, magnetoelastic, and magnetocrystalline interactions. Specific terms in Eq. (1.1) are then described. The final Section introduces relaxation measurements and defines decay time and viscosity as two measures of relaxation. Measurements of these quantities are reported in Chapter 4.

Symmetry and Irreducible Representations

Consider a physical characteristic possessed by a system with a particular symmetry. It can be shown that the operator which measures this property may be subdivided into orthogonal components, not all necessarily of the same dimensionality, each of which reflects one component of the symmetry of the system. If these components cannot be further decomposed into elements with lower symmetry they comprise *irreducible representations* of the operator. This notion is more easily grasped in mathematical form. If the symmetry operations R leave the system unchanged, then

$$RHy_i = H(Ry_i) = E_i(Ry_i)\,. \tag{1.2}$$

If this is true, then Ry_i is necessarily a linear combination of degenerate eigenstates with energy E_i, so that

$$Ry_j = \sum_i D_{ij}(R)y_i\;. \tag{1.3}$$

The matrices $D(R)$ form a representation of a group; if these matrices are transformed into maximally-symmetric block form, they form an irreducible representation of the group [20].

The notion of irreducible representations has special importance because of Neumann's principle, which states that any physical property of a crystal must have the symmetry of the point group of the crystal. This principle requires that an operator transform as the totally symmetric irreducible representation of the point group. Since the irreducible representations for the 32 point groups have long been tabulated, explicit eigenfunctions for any operator can immediately be constructed for any given crystal symmetry [22],[23]. These ideas find application in subsequent sections which introduce the elastic, magnetoelastic and magnetocrystalline Hamiltonians.

The Elastic Interaction

The important results of elasticity theory concern two neighboring points (at **r** and **r**+**a**) and how the distance between them varies as the body is deformed [24]. If a deformation displaces a point from **r** to **r**', then the displacement field is

$$\mathbf{u}(\mathbf{r}) = \mathbf{r}' - \mathbf{r} \, . \tag{1.4}$$

If the two points in the unstrained material differ in position by **a**,

$$d\mathbf{a} = \mathbf{u}(\mathbf{r}+\mathbf{a}) - \mathbf{u}(\mathbf{r}) \, . \tag{1.5}$$

By a Taylor expansion to first order, the components can be written

$$da_i = \sum_j \left(\frac{\P u_i}{\P x_j} \right) a_j \, . \tag{1.6}$$

The term in parenthesis may be separated into symmetric and antisymmetric parts; these represent the *strain* and *rotation,* respectively:

$$e_{ij} = \frac{1}{2}\left(\frac{\P u_i}{\P x_j} + \frac{\P u_j}{\P x_i} \right), \quad p_{ij} = \frac{1}{2}\left(\frac{\P u_i}{\P x_j} - \frac{\P u_j}{\P x_i} \right). \tag{1.7}$$

Hooke's law relate the stress to the strain, both tensors, so that

$$\begin{aligned} e_{ij} &= \sum_{kl} s_{ijkl} t_{kl} \ , \\ t_{ij} &= \sum_{kl} c_{ijkl} e_{kl} \ , \end{aligned} \tag{1.8}$$

which defines the elastic stiffness and compliance tensors, **s** and **c**. These expressions are usually simplified using the Voigt notation, by which pairs of indices (i,j) are replaced by a single symbol (m) according to the following: (1,1)→(1), (2,2) →(2), (3,3) →(3), (2,3) →(4), (3,1,) →(5), and (1,2) →(6). Although these forms assume a Cartesian representation, generalized analogues of the stress, strain, stiffness and compliance tensors can be appropriately generalized to (irreducible) representations for crystallographic point groups, using symmetry results of group theory as in Ref. ([25]).

Finally, the strain energy is obtained from the work done in creating the deformation. The work per unit volume needed to increase e_i by de_i is $dW = \sum_{ij} t_{ij} e_{ij}$, so that

$$W = \frac{1}{2}\sum_{i} c_{ij} e_i e_j . \tag{1.9}$$

This is valid for the Cartesian strains, but it can more generally be written as a sum involving the strain functions $e_i^{\Gamma,j}$ with $i = 1,2,\ldots,n$, which form the basis for the n-dimensional irreducible representation Γ,

$$H_{EL} = \sum_{\Gamma} \sum_{j,j'} \frac{1}{2} c^{\Gamma}_{jj'} \sum_{i} e_i^{\Gamma,j} e_i^{\Gamma,j'} . \tag{1.10}$$

Although this generality may seem unnecessary, in fact the opposite is true. The basis functions $e_i^{\Gamma,j}$ for the crystallographic point groups have been tabulated, and Callen and Callen have shown by applying symmetry arguments that the elastic and magnetoelastic interactions in the 32 point groups can be described by 11 irreducible Hamiltonians, which they tabulate [22]. Thus, the irreducible strains, elastic constants, and magnetoelastic Hamiltonians appropriate to a given crystal symmetry can be constructed directly from Eq. (1.10).

For Dy and the hcp rare earths, which have space group D_{3h}, the relevant irreducible strain components are related to the Cartesian strain components defined above by [22]:

$$
\begin{aligned}
e^{a,1} &= e_{11} + e_{22} + e_{33} \ , \\
e^{a,2} &= \frac{1}{2\sqrt{3}}\left[2e_{33} - e_{11} - e_{22}\right] , \\
e^{g,1} &= \frac{1}{2}\left[e_{11} - e_{22}\right] , \\
e_2^g &= e_{12} \ , \\
e_1^e &= e_{23} \ , \\
e_2^e &= e_{13} \ ,
\end{aligned}
\tag{1.11}
$$

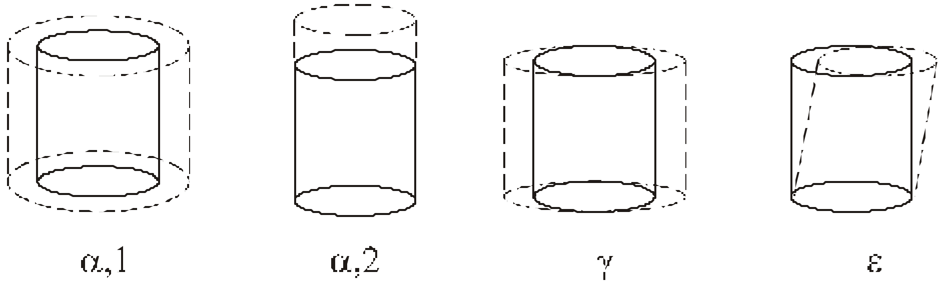

Figure 1.2. The normal modes of deformation of a hexagonal lattice. After Reference [26].26

and the irreducible elastic constants are

$$
\begin{aligned}
c_{11}^a &= \frac{1}{9}(2c_{11} + 2c_{12} + 4c_{13} + c_{33}) , \\
c_{22}^a &= \frac{2}{3}(c_{11} + c_{12} - 4c_{13} + 2c_{33}) , \\
c_{12}^a &= \frac{2}{3\sqrt{3}}(c_{13} + c_{33} - c_{11} - c_{12}) , \\
c^g &= 2(c_{11} - c_{12}) , \\
c^e &= 4c_{44} \ .
\end{aligned}
\tag{1.12}
$$

By inspection of Eq. (1.11), the irreducible strains clearly identify the normal mode deformations that are important to the hexagonal lattice, and these are shown as Figure 1.2. Values of these constants which are used in the calculations reported by Rosen and Klimer [27]; these appear in Table 1.1. Finally, the irreducible elastic Hamiltonian for Dy can be written

$$H_{EL} = \frac{1}{2}c_{11}^{a}(e^{a,1})^2 + c_{12}^{a}e^{a,1}e^{a,2} + \frac{1}{2}c_{22}^{a}(e^{a,2})^2 + \frac{1}{2}c^{g}[(e_1^{g})^2 + (e_2^{g})^2] + \frac{1}{2}c^{e}[(e_1^{e})^2 + (e_2^{e})^2] \ . \tag{1.13}$$

The elastic energy for Dy strained by growth along its b-axis on a Y/Lu alloy is shown as a function of a-axis strain in Figure 1.3. Note that, because of the closely similar c/a ratios of Y and Lu, Dy can be prepared with nearly-zero in-plane strain.

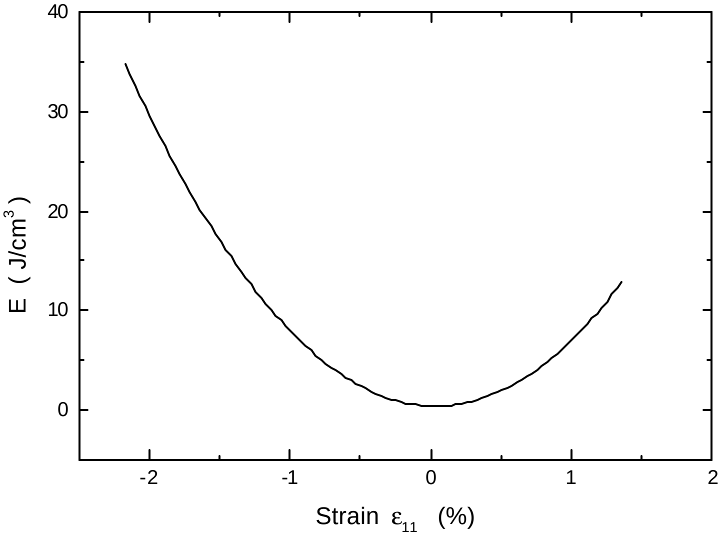

Figure 1.3. The elastic energy in Dy compressed or stretched by growth on Y/Lu alloys.

Constant	T = 10 K (J/cm^3)	T = T$_C$ (J/cm^3)
c_{11}^{a}	4.16 x 10^4	3.66 x 10^4
c_{22}^{a}	1.33 x 10^5	1.19 x 10^5
c_{12}^{a}	-5.39 x 10^2	6.43 x 10^3
c^{g}	1.12 x 10^5	1.09 x 10^5
c^{e}	1.08 x 10^5	1.05 x 10^5

Table 1.1. Irreducible elastic constants of Dy. T_C is 90 K for bulk Dy. After Ref. [27].

Magnetocrystalline Anisotropy

The crystal field term H_{CF} describes the Coulomb interaction between an ion of charge e embedded in an anisotropic charge distribution ρ (the “crystal field”) and the surrounding electrons and nuclei. The crystal field necessarily embodies the point symmetry of the local 4f site. The electrostatic potential energy is [18],

$$V_{CF} = \int \frac{er\ (\mathbf{R})}{|\mathbf{r}-\mathbf{R}|} d\mathbf{R} \ . \tag{1.14}$$

In analogy to the classical multipole expansion of Eq. (1.14), the crystal field operator H_{CF} is constructed in terms of an irreducible representation Γ of the appropriate point group,

$$H_{CF} = \sum_{\Gamma,i,l} B^{\Gamma,l} \mathbf{O}_i^{\Gamma,l}(\mathbf{J}) \ , \tag{1.15}$$

where **J** is the angular momentum operator, and **O** are the Stevens angular momentum operators, an operator analog of spherical harmonic functions.

Dy has hexagonal point symmetry. The symmetry arguments discussed in the previous section allow us to write

$$H_{CF} = \sum_i \left[\sum_{l=2,4,6} B_l^0 O_l^0(\mathbf{J}_i) + B_6^6 O_6^6(\mathbf{J}_i) \right] . \tag{1.16}$$

This can be converted into a real space representation using spherical harmonics:

$$\begin{aligned} H_{CF} = K_2 r^2 Y_2^0(q,f) + K_4 r^4 Y_4^0(q,f) + K_6 r^6 Y_6^0(q,f) + \\ + K_6^6 r^6 \left(Y_6^6(q,f) + Y_6^{-6}(q,f) \right) . \end{aligned} \tag{1.17}$$

The relative strength of the coefficients determines the easy axis of magnetization and eventually the detailed structure of the helimagnetic wave that comprises the antiferromagnetic state of Dy. Values of these coefficients are listed in Table 1.2. For Dy, the uniaxial coefficient K_2 is the dominant term and this confines the moments to the basal plane. Within the basal plane, the easy axis of magnetization is specified by K_6^6. The uniaxial anisotropy for Dy is shown in Figure 1.4, and the basal plane anisotropy is shown in Figure 1.5, both calculated from Eq. (1.17).

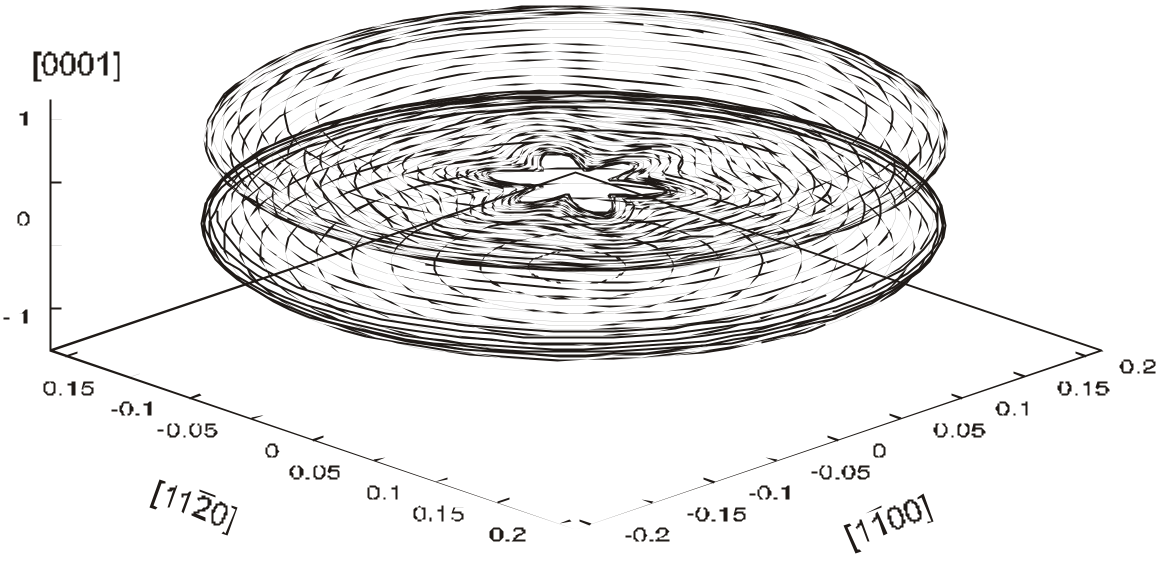

Figure 1.4. The magnetocrystalline anisotropy energy for Dy, showing the strong uniaxial anisotropy. The distance from the origin to a point on the surface is the energy associated with a moment pointing in that direction.

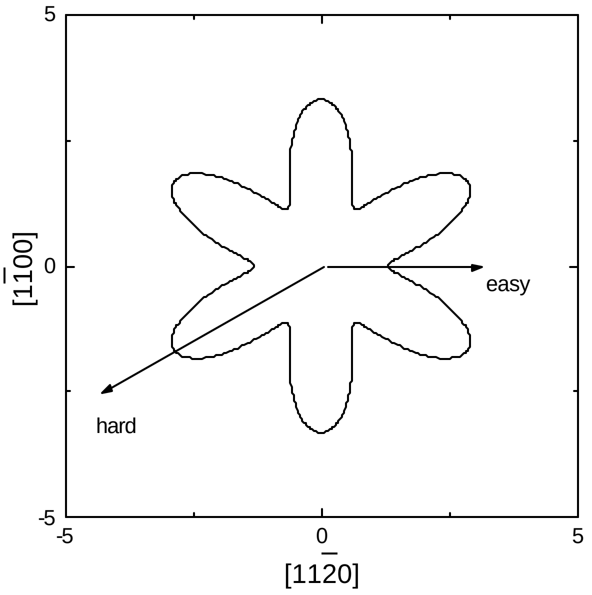

Figure 1.5. The magnetocrystalline anisotropy energy for Dy, in the basal plane. The directions of energy minima are the easy axes of magnetization.

	Constant (J / cm^3)
K_2	33.70
K_4	3.03
K_6	1.47
K_6^6	-0.80

Table 1.2. Magnetocrystalline coefficients of Dy. After Ref. [28].

Magnetoelastic Coupling

The magnetoelastic term H_{ME} describes the coupling between lattice strains and internal magnetic energy. For the rare earths the crystal field and exchange effects are the dominant contributions to energy, so the coupling constants are expanded in a Taylor series of the irreducible strain components,

$$\begin{aligned} H_{EX} &= \sum_{m,n} \left\{ J_{n,m} + \sum_{\Gamma,i} \left(\frac{\partial J_{n,m}}{\partial e_i^{\Gamma}} \right) e_i^{\Gamma} + \ldots \right\} (\mathbf{S}_n \cdot \mathbf{S}_m) , \\ H_{CEF} &= \sum_{\Gamma,i,l} \left\{ B_0^{\Gamma,l} + \left(\frac{\partial B^{\Gamma,l}}{\partial e_i^{\Gamma}} \right) e_i^{\Gamma} + \ldots \right\} \mathbf{O}_i^{\Gamma,l} , \end{aligned} \tag{1.18}$$

so that H_{ME} comprises the strain-dependent terms [29],

$$H_{ME} = \sum_{m,n} \left\{ \sum_{\Gamma,i} \left(\frac{\partial J_{n,m}}{\partial e_i^{\Gamma}} \right) e_i^{\Gamma} + \ldots \right\} (\mathbf{S}_n \cdot \mathbf{S}_m) + \sum_{\Gamma,i,l} \left\{ \frac{\partial B^{\Gamma,l}}{\partial e_i^{\Gamma}} e_i^{\Gamma} + \ldots \right\} \mathbf{O}_i^{\Gamma,l} . \tag{1.19}$$

Explicit forms of Eq. (1.19) for all crystallographic point groups are provided in Ref. [25]. For the case of metals with hexagonal symmetry, the lowest order energy with non-vanishing coefficients can be written most generally as

$$\begin{aligned} H_{ME} = {} & B_1^{a,0} e^{a,1} + B_1^{a,2} e^{a,1} (a_z^2 - \frac{1}{3}) + B_2^{a,0} e^{a,2} + B_2^{a,2} (a_z^2 - \frac{1}{3}) + \\ & + \frac{1}{2} B^{g,2} e_1^g (a_x^2 - a_y^2) + B^{g,2} e_2^g a_x a_y + \\ & + B^{e,2} e_1^e a_x a_y + B^{e,2} e_2^e a_x a_z \ , \end{aligned} \qquad (1.20)$$

where B_i and e_i are the irreducible magnetoelastic constants and strains, and the a_i are the direction cosines with respect to the *a* and *c* axes. For Dy in the ferromagnetic state, the moments are aligned parallel to the *a* directions and Eq. (1.20) is simply

$$H_{ME} = B^{a,1} e^{a,1} + B^{a,2} e^{a,2} + B^g e^l \ . \qquad (1.21)$$

The values of these constants are obtained by minimizing the total elastic and magnetoelastic energy and by using measured values of the Dy lattice paramters, as discussed further in Chapter 5; these appear in Table 1.3. The magnetoelastic energy for unstrained, compressed and stretched Dy appears in Figure 1.6. For stretched Dy, the in-plane *a*-direction becomes *a* direction of lowest energy. This is precisely the energy term which causes the spontaneous elongation of the a-directions as bulk Dy becomes ferromagnetic.

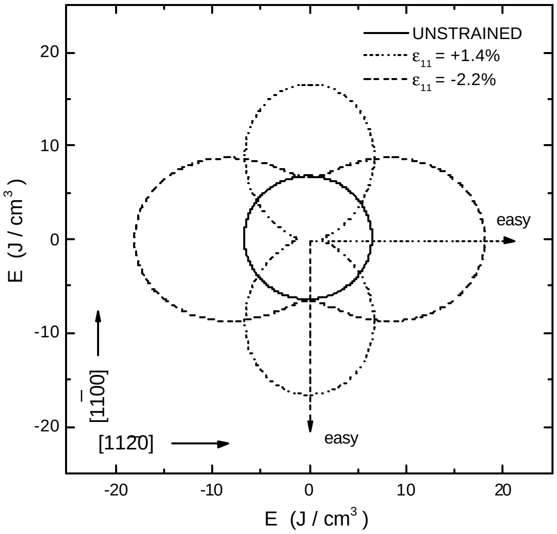

Figure 1.6. Magnetoelastic energy in Dy. For the stretched and compressed cases, the easy axis of magnetization is indicated.

	Constant (J/cm^3)
$B^{a,1}$	3.03
$B^{\alpha,2}$	1.47
B^{γ}	0.80

Table 1.3 Magnetoelastic coefficients of Dy at T=10 K.

Shape Anisotropy

The collection of magnetic dipoles which comprise a magnetized body gives rise to a self-energy [30],

$$E_S = \frac{1}{2} V \int_V \mathbf{M}(\mathbf{r}) \cdot \mathbf{H}_{\text{in}}(\mathbf{r}) d^3\mathbf{r}, \tag{1.22}$$

where **M** is the magnetization at **r’** in the body, V is the volume, and $\mathbf{H}_{\text{in}}$ is the internal magnetic field created by all other moments in the sample. The factor 1/2 avoids double-counting. For a uniformly magnetized body, the self-energy cancels throughout the interior, so that the important contributions to Eq. (1.22) arise from uncompensated magnetic dipoles on the surfaces, as shown in Figure 1.7. Thus, the self-energy depends on the shape of the magnetized volume.

There is no simple mathematical expression for the self-energy for all bodies. If the surface is described by a conic section, however, the internal field is uniform [30]. It is convenient to evaluate Eq. (1.22) for an ellipse, from which many shapes of physical relevance (sphere, cylinder, infinite sheet) may be considered limiting cases [31]. For an ellipse,

$$H_{\text{in}} = -\mathbf{D} \cdot \mathbf{M}, \tag{1.23}$$

where **D** is the demagnetizing tensor. (If **M** is parallel to one of the principal axis, the **D** is the scalar demagnetizing factor.) Substituting Eq. (1.23) into Eq. (1.22) gives

$$E_S = \frac{1}{2} V (N_{11} M_x^2 + N_{12} M_x M_y + \Lambda) , \qquad (1.24)$$

where $Tr\{N\} = 1$.

The subdivision of a magnetic body into subregions of uniform magnetization, known as magnetic domains, allows the total energy to be reduced [32]. This behavior is shown in Figure 1.7. The ellipsoids in Figures 1.7b and 1.7c are both fully magnetized, but that of Figure 1.7c has lower total energy due to partial cancellation of the uncompensated surface dipoles. Although not obvious, it is the long-range nature of the magnetostatic interaction which permits domain walls to reduce energy. Neighboring spins in the domain wall may have different orientations, and these will contribute to the shorter-range exchange energy, E_{EX}. The actual domain structure is therefore one in which the total energy, including shape and exchange, is minimized. This idea is discussed further in Chapter 5, in connection with domain walls in b-axis-oriented Dy.

The Zeeman Interaction

The simplest term in the magnetoelastic Hamiltonian is the interaction of a magnetic moment m in an external magnetic field **H**. This is described by the Zeeman Hamiltonian [33],

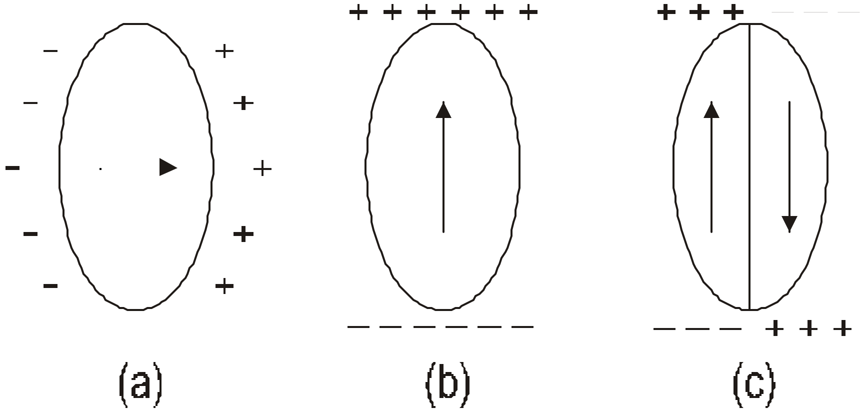

Figure 1.7. The origin of shape anisotropy. Magnetic dipoles are compensated throughout the volume, so that the self-energy depends on the uncompensated magnetic dipoles at the surfaces. Ellipsoid (a) has greater energy than ellipsoid (b), since uncompensated surface dipoles are spread over a larger area in (a). The energy of ellipsoid (c) is lower than (b), due to partial cancellation at

the surfaces.

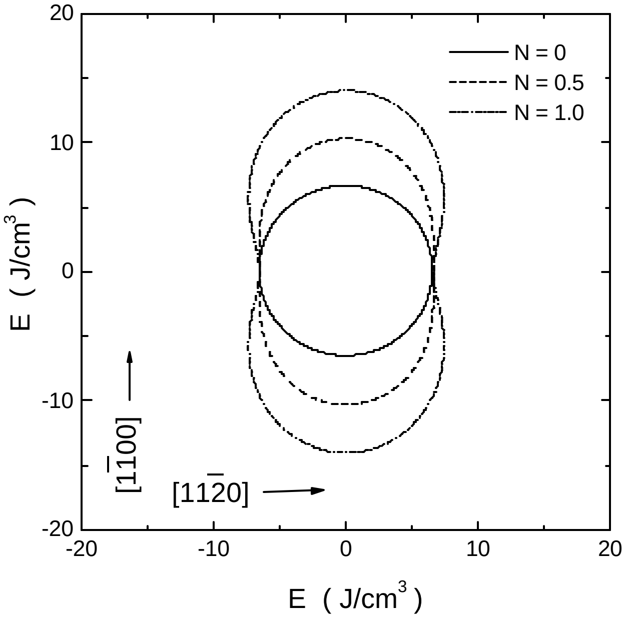

Figure 1.8. Shape anisotropy. As the demagnetizing factor increases, there is an increased cost in free energy for moments with a perpendicular magnetization component.

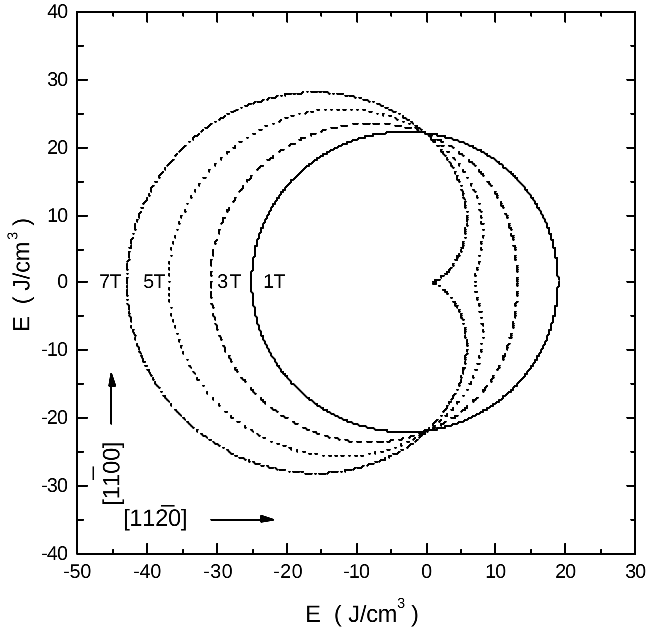

Figure 1.9. The Zeeman interaction, with the applied field along the [1120] axis.

$$H_Z = -m \cdot \mathbf{H} . \tag{1.25}$$

Because of the sign of Eq. (1.25), the state of lowest energy occurs for parallel alignment of the moment with the field. The energy for non-parallel alignment varies as the cosine of the angle between the moment and the field, as shown in Figure 1.9.

Indirect Exchange Coupling

The 4f core electrons are highly localized, so there is no significant exchange interaction directly between electrons on separate atoms. Instead, the dominant interaction is the indirect exchange interaction H_{EX}, which couples local moments through a polarization of the conduction electrons [34]. The interaction energy between two spins at $\mathbf{R}_n$ and $\mathbf{R}_m$ is given by the Heisenberg Hamiltonian,

$$H = -\sum_{n \neq m} J(\mathbf{R}_{nm})\mathbf{S}_n \cdot \mathbf{S}_m . \tag{1.26}$$

The coupling strength J is a complicated term approximately described by second order perturbation theory starting with wavefunctions obtained from electronic structure calculations [35]. However, the observed features of indirect exchange are adequately understood by the simpler RKKY (Ruderman-Kittel-Kasuya-Yosida) model [18]. In this model, an interaction similar to Eq. (1.26) between a core spin $\mathbf{S_q}$ and a conduction electron spin $\mathbf{s_{-q}}$ gives

$$J(\mathbf{q}) = \frac{2}{N}\left| j_{sf}(\mathbf{q}) \right|^2 c(\mathbf{q}) , \tag{1.27}$$

where j_{sf} is the interaction strength between *s*-like conduction states and the *f* core electrons, N is the number of magnetic lattice sites per unit volume, and χ is the generalized susceptibility. Assuming that j_{sf} is independent of $\mathbf{q}$, and using the free-electron form of χ, one obtains

$$c(\mathbf{q}) = \frac{2m_B^2}{V}\sum_{nn'k}\frac{f_{n\mathbf{k}} - f_{n'\mathbf{k}-\mathbf{q}}}{e_{n'}(\mathbf{k}-\mathbf{q}) - e_n(\mathbf{q})}. \tag{1.28}$$

The coupling term can be written

$$J(\mathbf{R}_{mn}) \propto \left|j_{sf}\right|^2 F(2k_F\left|\mathbf{R}_m - \mathbf{R}_n\right|), \tag{1.29}$$

where k_F is the momentum at the Fermi energy, and the function F is defined by

$$F(x) = \frac{x\cos x - \sin x}{x^4}. \tag{1.30}$$

Since j_{sf} is nearly isotropic and almost the same for all heavy rare earths, Eq. (1.28) shows that the largest contribution to J occurs for pairs of states with energies close to the Fermi level and separated by $\mathbf{q}$ [36],[37]. Such states are located at parallel (nesting) features of the Fermi surface. These nesting states contribute significantly to the complicated magnetic structures in rare earths, since Kohn anomalies in J($\mathbf{q}$) associated with these states give rise to long-range Friedel oscillations in the Fourier-transformed J($\mathbf{R}$). The form of J calculated for the rare earths is shown as Figure 1.10. The spatial extent of J is highly anisotropic, so that coupling along the [0001] direction is favored. Note that J can be either positive or negative. For example, in the AF state of Dy, moments within the basal planes are coupled ferromagnetically, but neighboring basal planes couple together antiferromagnetically.

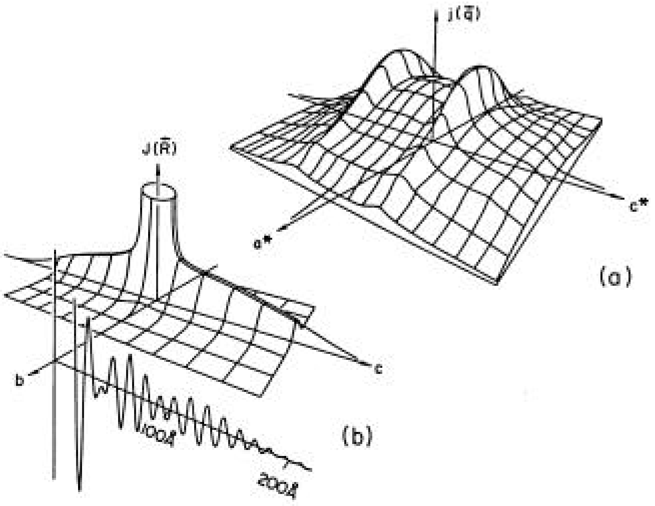

Figure 1.10. A schematic representation for the coupling J(q) and its Fourier transform J(R) in the rare earths. After Reference [35].35

1.4 Dysprosium

Dy, with L=5, S=5/2, and J=15/2, is an ideal rare earth for initial studies of the way the symmetry of the b-axis-orientation can be broken by epitaxy, and the way that magnetoelastic properties then affect magnetic behavior. First, its structural properties are favorable. Like Lu and Y it is a hcp metal, with lattice parameters which can be strained from a large compression of ε_{11}=-2.2% by growth on Lu, to a large tension of ε_{11}=+1.4% by growth on Y. Second, the PM-AF and AF-FM phase transitions occur at easily accessible temperatures of T_N = 178 K and T_C = 85 K, respectively. The way magnetic order depends on temperature and applied field is shown in Figure 1.11. Finally, the magnetic configuration is simple and well-suited to growth in the b-axis-orientation. The AF state has a simple spiral arrangement of ferromagnetic basal planes, each magnetized transversely and successively rotated by a constant turn angle. The FM state also has a simple arrangement with all moments pointing along just one of the equivalent a-axes. In both the AF and FM phases, the strong magnetocrystalline anisotropy restricts the moments to lie in the basal plane, preferring the six equivalent a-axes of easy magnetization. As shown in Chapter 4, simple and easily controlled modifications of this magnetic order can be achieved by growth of Dy in the b-axis-orientation.

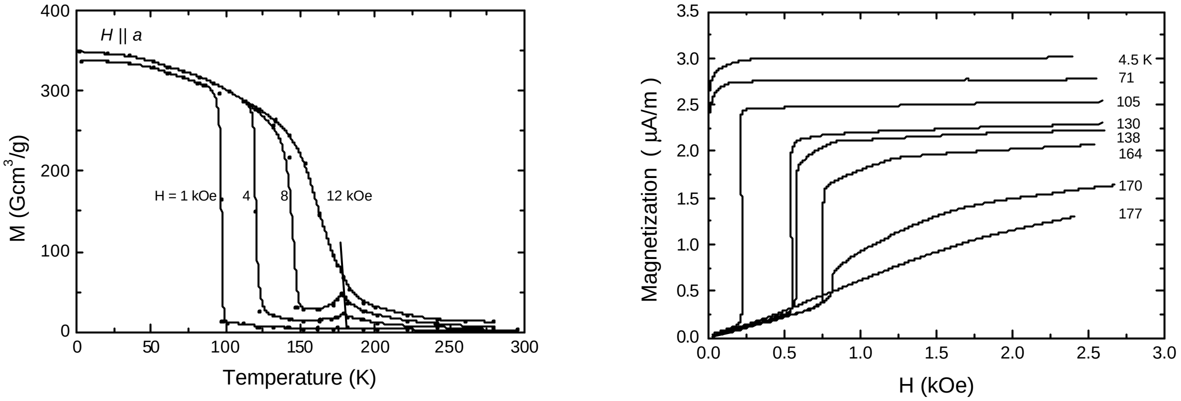

Figure 1.11. The temperature- and field-dependent magnetic ordering in bulk Dy.

The AF-FM Phase Transition at Zero Field

The Curie temperature of T_C = 85 K marks the AF-FM phase boundary in zero field for bulk Dy. Above T_C, the Dy crystal structure is hexagonal-close-packed. The oscillatory exchange interaction couples moments within basal planes ferromagnetically, but the direction of successive planes differs by a temperature-dependent turn angle which becomes 30° just above T_C, and this forms the helix shown in Figure 1.1. Below T_C Dy undergoes an orthorhombic lattice distortion with $\Delta a / a=+0.2\%$, $\Delta b / b=-0.5\%$, $\Delta c / c=+0.3\%$, as shown in Figure 1.12. In each ferromagnetic domain the magnetization is oriented along one of the six equivalent a-axis directions. With parallel and antiparallel orientations of each magnetic domain causing equal magnetostriction, bulk Dy deforms into a mosaic of three-fold structural domains, as shown in Figure 1.12.

The quantitative application of magnetoelastic theory to an explanation of the zero-field AF-FM phase transition of bulk Dy is one of the successes of the local-moment model of rare earth magnetism; nevertheless, mathematical details still remain in dispute (see below). An extension of these ideas to c-axis-oriented epitaxial rare earth systems has met with similar success [38].

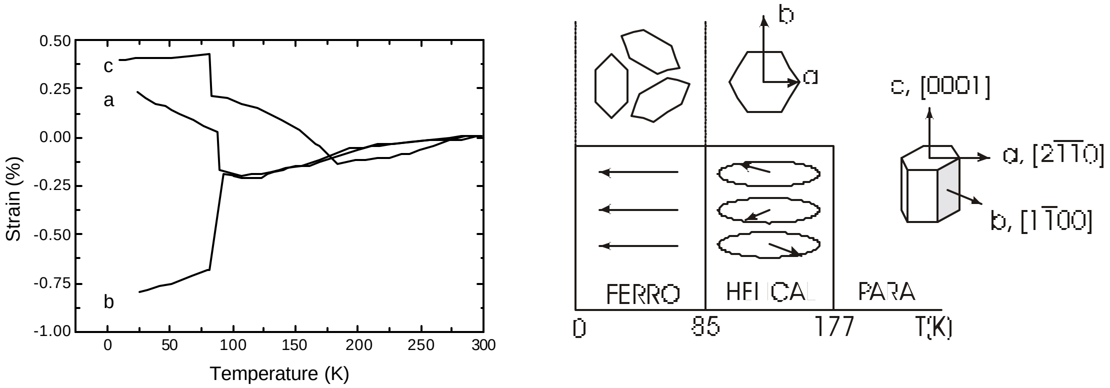

Figure 1.12. (Left) Temperature-dependence of the lattice parameters in bulk Dy. (Right) The magnetic domain structure of bulk Dy.

As first observed by Cooper, the exchange coupling term H_{EX} favors the antiferromagnetic (helimagnetic) configuration for all temperatures [39]. Therefore a collapse of the antiferromagnetic spin wave into the **q**=0 state accompanies the transition and but does not cause it. (In principle, J(**q**) retains a maximum at a non-zero, incommensurate **q** in the ferromagnetic state.) Below the Curie temperature T_C, however, there is a strong reduction in energy due to magnetostriction, principally with cylindrical symmetry, associated with the lowest-order magnetostriction effects. Because of spin-orbit coupling and the strong anisotropy of the 4f charge distribution, the magnetic spins and the crystal lattice are coupled so that the energy may be reduced by deforming the lattice. This reduction in magnetoelastic free energy below T_C more than compensates for the unfavorable ferromagnetic arrangement, and this drives the ferromagnetic transition [40].

The calculation of this driving energy from first principles is difficult. The quantitative model first proposed by Enz included explicitly the exchange interaction with just three planes interactioning, so that the driving energy is

$$E_{EX} = J_0 + 2J_1 \cos q + 2J_2 \cos 2q \,, \tag{1.31}$$

in which θ is the interplanar turn angle in the antiferromagnetic phase [41]. Most recently, Dumesnil and co-workers evaluated Eq. (1.31) while incorporating the epitaxial clamping constraint. By using the experimentally-measured interplanar turn angle, they were able to estimate the driving energy as a function of temperature for the c-axis Dy system.

Unfortunately, the actual exchange coupling is a long-range interaction which is not adequately described by Eq. (1.31). In 1977, Del Moral and Lee re-analyzed the known bulk magnetic data for Dy, incorporating new measurements of the AF coupling at different temperatures [42]. They found that the three plane interaction model contains fallacious assumptions such that any agreement with experiment is fortuitous. Two principal difficulties are identified by these authors. First, the exchange coupling is a long range interaction and therefore it is necessary to include many terms, not just two, in the expansion of H_{EX}. In fact, choosing only two variables to parameterize this interaction leads to an unphysical temperature dependence of the coefficients, which makes the validity of any conclusions derived from this model highly-questionable. Second, this formalism assumes that the exchange interaction does not change at the ferromagnetic transition. However, it is clearly apparent that the AF state causes new periodicities in the conduction band, through s-f coupling, which introduce superzone boundaries with states separated by an energy gap. This has been corroborated in neutron studies of the spin-wave dispersion in Dy [43]. These effects modify the electronic structure and consequently the exchange interaction also.

Finally, although the specific three-layer interaction model may be inadequate to describe the free energy of the antiferromagnetic state, it nevertheless remains true that the first order AF-FM phase transition is driven by the magnetoelastic energy associated with the reduction of the hexagonal symmetry of the basal plane. Chapter 5 discusses a calculation of the AF-FM driving energy, based on a model proposed by Erwin, which avoids these difficulties [38].

The AF-FM Phase Transition at Non-Zero Fields

Bulk Dy in zero field undergoes a spontaneous first-order transition to a ferromagnetic state at the Curie temperature of $T_C = 85$ K. However, an applied field can force bulk Dy into the ferromagnetic state at still higher temperatures, as seen in the field-induced magnetization *M(H)*, shown in Figure 1.11 [44],[45][46]. For temperatures below about 130 K, an external magnetic field can force the metal into the ferromagnetic state directly, and for temperatures between 130 K and T_N, an applied field can collapse the helical antiferromagnetic state into a distorted helix or “fan” state [47]. This process is shown as Figure 1.13, and the relevant phase diagram appears as Figure 1.14.

The critical field H_C reflects the difficulty with which the applied field forces the moments to realign. It is at once obvious that H_C must depend on the magnetic anisotropy. The relationship between H_C and temperature is, however, less clear. With increasing temperature the moments are, for example, better able to cross energy barriers by thermal activation, but this does not explain the reduction in H_C with increasing temperature above 130 K. A number of authors examined this behavior, and a consistent model by Nagamiya, Kitano and co-workers emerged to explain the dependence of H_C on temperature in bulk Dy [48],[49],[50]. This model has considerable intrinsic merit because it shows how well the local moment theory of magnetism can predict the complicated magnetic phase relationships that occur in the rare earths. In what follows this model is briefly reviewed, to facilitate its application to b-axis-oriented Dy in Chapter 5

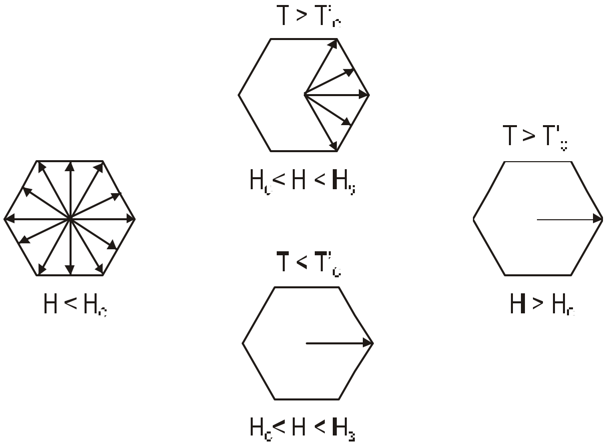

Figure 1.13. The effect of an applied magnetic field on the AF phase of bulk Dy. Below about 130 K, the field can force a FM state directly. Above this temperature, there is an intermediate “fan” state.

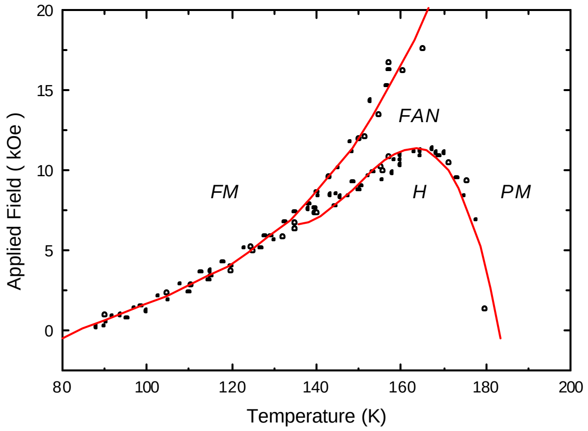

Figure 1.14. The magnetic phase diagram of bulk Dy, determined from magnetoresistance data, which identifies the ferromagnetic (FM), helical (H), paramagnetic (PM) and fan states.. After Reference [51].51

In bulk Dy the antiferromagnetic state is characterized by a helical structure in which basal planes are each ferromagnetically ordered, with the magnetization of successive basal planes reoriented by a “turn angle.” This angle is in general not commensurate with the lattice, so that the moments do not occur at the precise minima predicted from the magnetocrystalline anisotropy. The simplest Hamiltonian which describes this situation includes exchange, magnetocrystalline anisotropy, and Zeeman coupling [52]:

$$H = H_{EX} + H_{CF} + H_Z \quad . \tag{1.32}$$

The mathematical analysis is complicated, but the key results are 1) a modified critical field given in terms of the spin S, anisotropy coefficient K_6^6 and moment μ by

$$H_C = H_C^0 - 2\left|K_6^6\right|S^6 \; / \; m , \tag{1.33}$$

which is reduced from the critical field H_C^0 that describes the behavior in the absence of anisotropy; and 2) the phase diagram shown as Figure 1.15, given in terms of the reduced (scaled) anisotropy and applied field parameters [53]:

$$X = \frac{2m\left|K_6^6\right|S^6}{2g_j m_B S^3[J(Q) - J(0)]} ,$$
$$Y = \frac{mH}{2S^2[J(Q) - J(0)]} . \tag{1.34}$$

Here g is the Landé factor. The phase diagram in Figure 1.15 shows that an applied field induces either a first-order ferromagnetic transition or else a second-order fan transition, depending on the magnitude of the planar anisotropy. Sufficiently large fields always create the ferromagnetic state, as expected.

As discussed in Ref. [51], this phase diagram, together with experimental measurements of the magnetocrystalline planar anisotropy coefficient K_6^6, provides an explanation for the temperature dependence of H_C shown in Figure 1.14. The coefficient K_6^6 is known to decrease with temperature [28]. Up to 130 K, K_6^6 is sufficiently large that X is greater than X_1 and so a first-order transition takes place from the helical to ferromagnetic state. Above 130 K, X falls below X_1 and this introduces a temperature-dependent fan state above H_C. The simple basis developed for Eq. (1.32) and following demonstrates the success the local-moment picture achieves in describing rare earth magnetism.

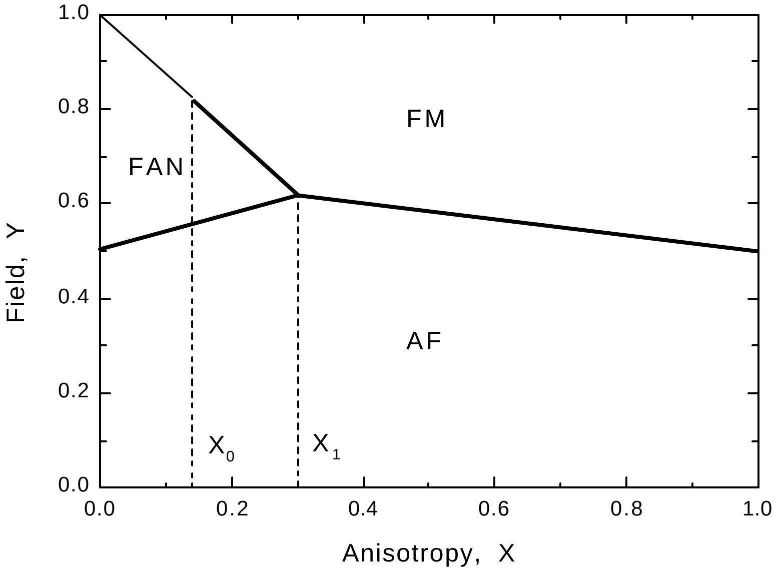

Figure 1.15. Calculated phase diagram for bulk Dy, showing how an applied field (Y) can induce either ferromagnetic or fan state transitions, depending on the magnitude of the planar anisotropy (X). Here X and Y are reduced quantities, defined in Eq. (1.34). The thin lines denote a second-order phase transition, and the thick lines denote a first order phase transition.After Reference [53].53

The AF-FM Phase Transition and External Stress

Strain has been used as a control parameter to probe the AF-FM phase transition. The first experiments in bulk, single-crystal Dy were performed by Bartholin et al., using hydrostatic and uniaxial stress [54]. These authors found that the Curie temperature decreased with increasing hydrostatic stress. The Curie temperature increased with increasing uniaxial stress applied along the hexagonal a and b axes, but decreased along the c-axis. The results of these experiments are shown as Figure 1.16.

More recently, a variation in T_C with strain was discovered in epitaxial Dy. For compressed c-axis-oriented Dy grown on Lu, the Curie temperature was enhanced; for stretched c-axis-oriented Dy grown on Y, the AF-FM phase transition was completely suppressed and the samples remained antiferromagnetic in zero field. The complete phase diagram for this behavior in c-axis-oriented Dy was first reported by Tsui and Flynn, and it appears as Figure 1.16 [55]. When the appropriate strains are calculated, the enhancement or suppression of T_C with strain in the epitaxial case agrees qualitatively for that observed in bulk pressure experiments.

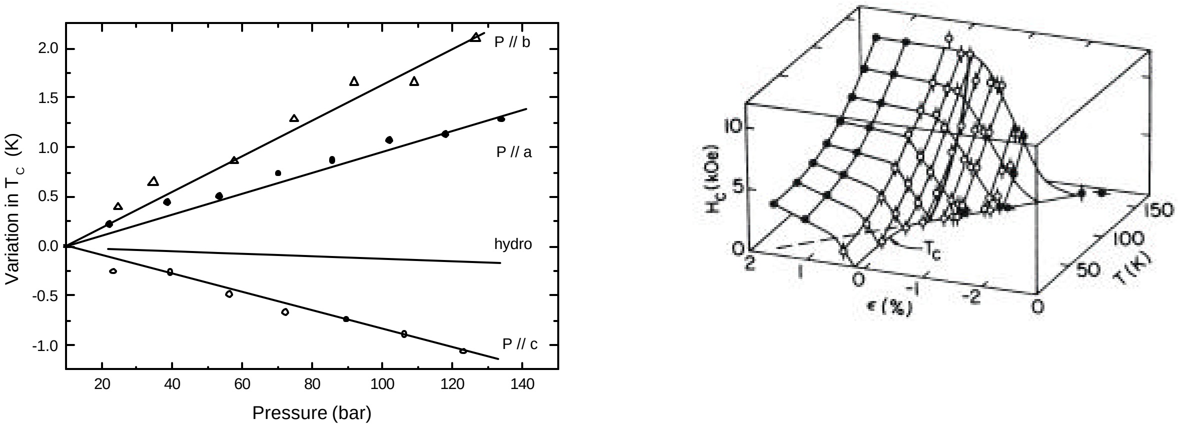

Figure 1.16. The variation of the Curie temperature T_C with uniaxial and hydrostatic pressure in bulk Dy (left), and the epitaxial phase diagram for c-axis-oriented Dy (right).

A theoretical analysis of the variation of T_C with strain for epitaxial rare earths was first proposed by Erwin, who suggested that the effect of strain on the magnetoelastic energy over- or undercompensates the exchange energy which favors the antiferromagnetic state [38]. This argument qualitatively predicts the observed enhancement or suppression of the AF-FM transition. In Chapter 5, these ideas are applied to show that the phase behavior of b-axis-oriented, c-axis-oriented, and bulk Dy can be understood with a single model and the same material-dependent parameters. Moreover, this model is extended so that, for the first time, the transition temperature can be quantitatively coupled to the measured strains.

1.5 Magnetic Domains and Intrinsic Coercive Fields

A magnetic system can lower its overall free energy by separating into a collection of spatially-discrete but dipole-coupled domains, each uniformly magnetized. The magnetization of a sample can therefore change either by domain wall movement, or by a combination of domain growth and coherent rotation of the moments inside domains. The existence and motion of domain walls gives rise to non-zero coercive fields which derive from two basic mechanisms associated with domain walls. These are intrinsic coercive fields and coercive fields due to domain wall pinning. This Section reviews a calculation of domain structure and intrinsic coercive fields published by Egami and Graham [56]. This will be of use later in interpreting the coercive fields measured for b-axis-oriented Dy and discussed in Chapter 5.

Observations are lacking for domain walls in bulk and thin film Dy [57], [58]. For bulk Dy, however, the strong exchange coupling in the basal plane (even in the AF state the basal plane remains ferromagnetic) suggests that the domain structure comprises 180° domain walls which run parallel to the (0001) basal planes [56]. The magnetization can rotate freely *between* basal planes and so these are likely to be Bloch walls with the axis of rotation perpendicular to the domain wall. Domains walls parallel to $(11\bar{2}0)$ planes are less likely, owing to strong ferromagnetic coupling in the basal plane, but they could also exist [59].

Egami and Graham have calculated the energetics associated with 180° domain walls aligned with the basal planes in Dy and Tb [56]. They have shown that these walls give rise to an intrinsic coercive force which depends on exchange, magnetocrystalline, and magnetoelastic anisotropy [56],[60]. The origin and nature of these coercive fields is clarified from the following calculation. The energy E_m of a domain wall comprises three terms,

$$E_m = -\sum_i J_{i,i+k}\mathbf{S}_i \cdot \mathbf{S}_{i+k} + \sum_i K_6^6 \cos 6q + \sum_i B^g e^g \cos 2q \,. \tag{1.35}$$

These are the interlayer exchange coupling (taken up to the fourth nearest-neighbor plane exchange), the sixfold magnetocrystalline basal plane anisotropy, and the uniaxial magnetoelastic energy. The calculated domain wall configuration is the stable spin configuration shown in Figure 1.17, obtained by an iterative method which adjusts q_i until the torque t_i acting on the i-th layer [56], namely,

$$t_i = -\P E_m / \P q \ , \tag{1.36}$$

is negligibly small. There are two principal results of this calculation. First, the domain wall thickness in Dy is approximately 7 atomic planes (20 Å) and the domain wall energy is about 5 erg/cm^2 (or 42 K/line of spins). In contrast, domain walls in transition metal ferromagnets are typically hundreds of atomic layers thick, and the domain wall energies are typically several times lower.

Second, the possible 180° domain walls fall into two general classes, as shown in Figure 1.17: domain walls with a plane of spins in the center of the wall which are oriented at 90° to the ferromagnetic axis (type A), and domain walls with the center of the wall falling between two spins (type B). Type B domain walls are the stable configuration; type A domain walls are metastable. However, for a domain wall to move in response to an applied field, the type B configuration must pass through the type A configuration. Since these states have different energy, this gives rise to an intrinsic coercive force, in analogy to the Peierls-Nabarro force on a dislocation in a crystal lattice. This coercive force is related to the energy difference between the two states,

$$m H_c \approx (p / 2)\Delta E_{A-B} . \tag{1.37}$$

The intrinsic coercive fields for Dy are calculated to be about 1 kOe, in good agreement with experiment [60]. This differs negligibly from the coercive fields for stretched b-axis-oriented Dy, reported in Chapter 4.

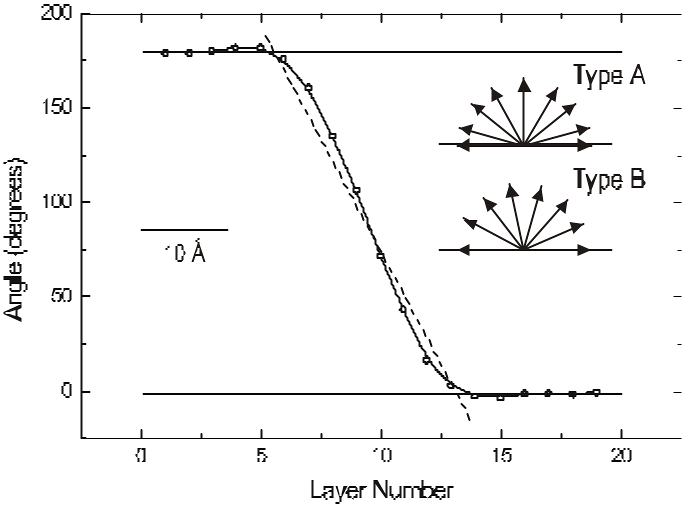

Figure 1.17. The calculated spin structure of a 180° domain wall in bulk Dy. The dotted line is the resulting spin structure when the effects of magnetocrystalline anisotropy and magnetostriction were ignored. The inset shows the two possible spin configurations in the domain wall. After Reference [56].56

1.6 Magnetic Relaxation Phenomena

Chapter 4 reports measurements of the magnetic properties of b-axis-oriented Dy performed as a function of temperature in small aligning fields, and also isothermal measurements of hysteresis in strong applied fields. The time-dependence of the magnetic response to an applied field was also measured. This Section introduces time-dependent magnetic effects and a convenient means for characterizing the time-dependence, used in Chapter 4.

Time-dependent magnetization effects have long been observed. One such effect is disaccomodation, or a time-dependence of permeability, possibly due to diffusive atomic rearrangement in response to local magnetization [61]. Another is the common magnetic aftereffect (also called magnetic creep), manifest as an exponential response of magnetization to a sudden change of applied field [62]. Creep is due in part to the retardation of domain wall motion or the rotation of coherent domains. The magnetization response is a complicated superposition of many processes, including domain wall motion, Barkhausen jumps, damping due to internal eddy currents, etc. [63].

Domain wall motion (or the rotation of coherent domains) can be a thermally-activated process at high temperatures or a quantum mechanical process at low temperatures. The idea that magnetization can involve a tunneling of spins between states is an old one, and a detailed theory of this process in rare earths is long established [64],[65]. There has been renewed interest in this phenomena for two reasons. First, the quantum tunneling of magnetization (QTM) provides an example of macroscopic quantum tunneling (MQT), a topic of high current interest, [66]. An example of this is flux creep in high-temperature superconductors at low temperature, where one flux quantum comprising many Cooper pairs in the surrounding screening current forms a macroscopic object that is thought to tunnel between pinning sites [67]. Second, QTM has some practical importance, since emerging magnetic technologies (such MRAM and spin-valve devices) are based on ultrasmall, magnetically-coherent structures for which tunneling effects may be important [68].

Magnetic moments realign in response to an applied field. In one model of this process, the moments are each initially confined to equilibrium states of minimum energy and, in an applied field, they must overcome energy barriers to reach a new stable configuration. Transitions between states occur in two ways. For sufficiently high temperatures, the energy barrier ΔE between minima is overcome by thermal activation (TA) and the transition rate is given by the Arrhenius law,

$$\Gamma = \Gamma_C \exp(-\Delta E / k_B T), \tag{1.38}$$

which is the product of a classical attempt frequency Γ_C with the Boltzmann factor [69]. For suitably low temperatures quantum tunneling between states of magnetization (QTM) may be the dominant process and this is described by a similar but non-thermal exponential form [70],

$$\begin{aligned} \Gamma &= \Gamma_Q \exp(-B) , \\ &= \Gamma_Q \exp(-\Delta E / \eta w_0), \end{aligned} \tag{1.39}$$

where the Gamov exponent B depends on the depth of the well and the initial frequency of oscillation of the particle in the well, ηw_0. The crossover temperature T_c^* between TA and QTM processes, shown in Figure 1.18, is defined by equating the exponential factors,

$$T_c^* = \frac{\Delta E}{k_B B}. \tag{1.40}$$

Generally, claims of magnetic quantum effects must be handled with care, due to the complicated temperature-dependence which magnetic systems may possess. As cited in Ref. [68], Oseroff measured extrapolated a non-zero intercept in a system with a linear magnetization behavior. This would appear to be evidence of QTM, but the system was later shown to depend on temperature as $T^{1/2}$ and insufficient data were collected at low temperatures to verify this.

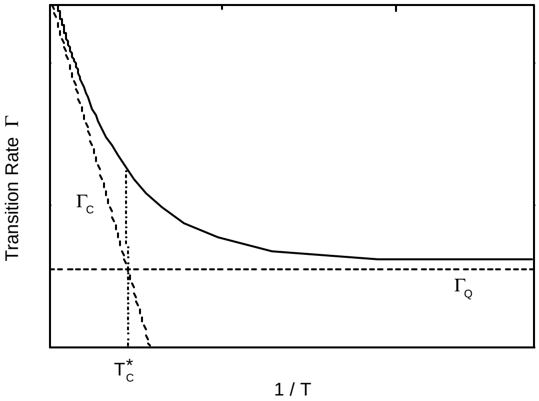

Figure 1.18. The temperature-dependent transition rate, showing the crossover from the thermally-activated (TA) regime at high temperatures to the quantum tunneling regime (QTM) below T_C*.

Characterizing Magnetic Relaxation

There are two common ways of characterizing magnetic relaxation measurements, magnetic exponential decay and magnetic viscosity; both are used in Chapter 4. Since most decay phenomena are exponential, one may expect an exponential time-dependence such as [71]

$$M(t) = M(0)\exp(-t \ / \ t) . \tag{1.41}$$

However, many magnetic systems are characterized by a distribution of decay times, so that [30],[72]

$$M(t) = M(0)\int_0^\infty P(t)\exp(-t \ / \ t)dt \ . \tag{1.42}$$

In many cases, Eq. (1.42) can be approximated by [73],[74]

$$M(t) = C - S\log(t \ / \ t) , \tag{1.43}$$

which defines the magnetic viscosity S as the logarithmic time derivative of magnetization,

$$S = dM \ / d\log t . \tag{1.44}$$

These two methods for representing experimental data are only approximate, however, owing to the fact that kinetics may be complicated in real magnetic systems.

References

[1] E. Salje, *Phase transitions in ferroelastic and co-elastic crystals* (University Press, Cambridge, 1990).

[2] R. Ramesh, *Thin film ferroelectric materials and devices* (Kluwer, Boston, 1997).

[3] See, for example, Y. Mimura, N. Imamura, *App. Phys. Lett.* **28**, 746 (1976); P. Chaudhari, J. J. Cuomo, R. J. Gambino, *App. Phys. Lett.* **22**, 337 (1973); R. J. Gambino, *AIP Conf. Proc.* **18**, 578 (1973).

[4] P. F. Carcia, *J. App. Phys.* **63**, 5073 (1988); H. J. G. Draaisma, W. J. M. de Jonge, F. J. A. den Broeder, *J. Mag. Mag. Mat.* **66**, 351 (1987); P. F. Carcia, A. D. Meinhaldt, A. Suna, *App. Phys. Lett.* **47**, 178 (1985).

[5] For references, see J. Ankner, J. A. Borchers, R. F. C. Farrow, R. F. Marks, *J. App. Phys.* **73**, 6427 (1993).

[6] M. Huth, C. P. Flynn, preprint.

[7] G. P. Bordallo, A. Mahoui, J. Lapasset, J. Moret, *Ferroelectrics* **190**, 57-63 (1997).

[8] J. Eckstein and J. O'Donnell, private communication.

[9] R. Du, F. Tsui, C. P. Flynn, *Phys. Rev. B* 2941-2943 (1988).

[10] J. Kwo, E. M. Gyorgy, D. B. McWhan, M. Hong, F. J. Disalvo, C. Vettier, J. E. Bower, *Phys. Rev. Lett.* **55**, 1402 (1985).

[11] For an authoritative review, see C. P. Flynn, M. B. Salamon, in *Handbook on the Physics and Chemistry of Rare Earths,* K. A. Gschneidner, L. Eyring, eds. (Elsevier, Amsterdam, 1996), 1.

[12] C. Durfee, private communication.

[13] M. J. Conover, A. Kaldowski, C. P. Flynn, *Phys. Rev. B* **53**, 2983 (1996).

[14] F. Tsui, C. P. Flynn, M. B. Salamon, R. W. Erwin, J. A. Borchers, J. J. Rhyne, *Phys. Rev. B* **43**, 13320-13330 (1991).

[15] K. Theis-Broehl, K. A. Ritley, C. P. Flynn, K. Hamacher, H. Kaiser, J. J. Rhyne, *J. App. Phys.* **79**, 4779-4781 (1996).

[16] K. Theis-Broehl, K. A. Ritley, C. P. Flynn, J. E. Van Nostrand, Klaus Hamacher, Helmut Kaiser, and J. J. Rhyne, *J. Mag. Mag. Mat..* **166**, 27-37 (1997).

[17] R. Du, Ph.D. thesis, Univ. Illinois, 1990.

[18] J. Jensen, A. R. Mackintosh, *Rare earth magnetism* (Oxford, Oxford, 1991).

[19] H. J. Zeiger, G. W. Pratt, *Magnetic interactions in solids* (Clarendon, Oxfold, 1973).

[20] G. Burns, *Introduction to group theory with applications* (Academic, New York, 1977).

[21] In contrast, for the 3d transition-metal magnets such as Fe and Co the itinerant electrons provide weak screening and a weak spin-orbit coupling; thus $H_{CF} > H_{SO}$, as is manifest in the point symmetry of their band structure.

[22] E. R. Callen, H. B. Callen, *Phys. Rev.* **129**, 578 (1963); E. Callen, H. B. Callen, *Phys. Rev.* **139**, A455 (1965).

[23] M. F. C. Ladd, *Symmetry in molecules and crystals* (Horwood, Chichester, 1989).

[24] See, for example, J. F. Nye, *Physical properties of crystals* (Clarendon, Oxford, 1955); A. E. H. Love, *A treatise on the mathematical theory of elasticity* (University Press, Cambridge, 1892); R. V. Southwell, *An introduction to the theory of elasticity* (Clarendon, Oxford, 1936); W. J. Ibbetson, *An elementary treatise on the mathematical theory of perfectly elastic solids* (Macmillan, New York, 1887).

[25] E. T. de Lacheisserie, *Magnetostriction* (CRC Press, Boca Raton, 1993).

[26] A. E. Clark, B. F. DeSavage, R. Bozorth, *Phys. Rev.* **138**, A216 (1965); A. E. Clark, B. F. DeSavage, R. Bozorth, *Phys. Letters* **5**, 100 (1963).

[27] M. Rosen, H. Klimer, *Phys. Rev. B* **1**, 3748 (1970).

[28] J. J. Rhyne, in *Magnetic properties of the rare earth metals*, R. J. Elliott, ed. (Plenum, London, 1972).

[29] A. del Moral, in *Magnetoelastic effects and applications*, L. Nanotte, ed. (Elsevier, Amsterdam, 1993).

[30] A. Aharoni, *Introduction to the theory of ferromagnetism* (Clarendon, Oxford, 1996).

[31] In fact, the Brown-Morrish theorem states that any uniformly magnetized body has the same internal energy as an ellipsoid of identical volume.

[32] P. Weiss, *Compt. Rend.* **143**, 1136-1139 (1906); P. Weiss, *J. de Physique* **6**, 661-690 (1907).

[33] R. Shankar, *Principles of quantum mechanics* (Plenum, New York, 1980).

[34] B. Coqblin, *The electronic structure of rare earth metals and alloys* (Academic, London, 1977).

[35] A. J. Freeman, in *Magnetic properties of rare earth metals,* R. J. Elliot, ed. (Plenum, London, 1972).

[36] T. Kasuya, in *Magnetism IIb*, G. T. Rado, H. Suhl, eds. (Academic, New York, 1965).

[37] S. H. Liu, R. P. Gupta, S. K. Sinha, *Phys. Rev. B* **4**, 1100 (1971).

[38] R. W. Erwin, J. J. Rhyne, J. Borchers, M. B. Salamon, R. Du, C. P. Flynn, in *Neutron scattering for materials science*, v. 166 (Materials Research Society, Pittsburgh, 1990).

[39] B. R. Cooper, *Phys. Rev. Lett.* **19**, 900 (1967); B. R. Cooper, *Phys. Rev.* **169**, 281 (1968).

[40] W. E. Evenson, S. H. Liu, *Phys. Rev.* **178**, 783 (1969).

[41] U. Enz, *Physica* **26**, 698-699 (1960).

[42] A. del Moral, E. W. Lee, *J. Phys. C: Solid State Phys.* **8**, 3881 (1975).

[43] R. M. Nicklow, N. Wakabayashi, M. K. Wilkonson, R. E. Reed, *Phys. Rev. Lett.* **26**, 140 (1971).

[44] J. J. Rhyne, S. Foner, E. J. McNiff, R. Doclo, *J. App. Phys.* **39**, 892-893 (1968).

[45] R. M. Bozorth, R. J. Gambino, A. E. Clark, *J. App. Phys.* **39**, 883-886 (1968).

[46] D. R. Behrendt, S. Legvold, F. H. Spedding, *Phys. Rev.* **109**, 1544-1547 (1957); J. F. Elliott, S. Legvold, F. H. Spedding, *Phys. Rev.* **94**, 1143-1145 (1954).

[47] M. Akhavan, H. A. Blackstead, P. L. Donoho, *Phys. Rev. B* **8**, 4258-4261 (1973).

[48] For an excellent review of this work, see B. Coqblin, *The electronic structure of rare-earth metals and alloys: the magnetic heavy rare-earths* (Academic Press, London, 1977).

[49] B. R. Cooper, in *Magnetic properties of the rare earth metals*, R. J. Elliott, ed. (Plenum, London, 1972).

[50] T. Nagamiya, K. Nagata, Y. Kitano, *Prog. Theor. Phys.* **27**, 1253 (1962).

[51] B. Coqblin, *The electronic structure of rare-earth metals and alloys: the magnetic heavy rare-earths* (Academic Press, London, 1977), p. 127.

[52] B. R. Cooper, R. J. Elliott, *Phys. Rev.* **131**, 1043 (1963); B. R. Cooper, R. J. Elliott, *Phys. Rev.* **153**, 654 (1967).

[53] Y. Kitano, T. Nagamiya, *Prog. Theor. Phys.* **31**, 1 (1964).

[54] H. Bartholin, J. Beille, D. Bloch, P. Boutron, J. L. Féron, *J. App. Phys.* **42**, 1679-1688 (1979).

[55] F. Tsui, C. P. Flynn, *Phys. Rev. Lett.* **71**, 1462-1465 (1993).

[56] T. Egami, C. D. Graham, *J. App. Phys.* **42**, 1299-1300 (1971).

[57] Magnetic force microscopy could be used, in principle, to make such measurements, but the available MFM apparatus at the University of Illinois does not have a low-temperature stage necessary to achieve a ferromagnetic state.

[58] See, for example, R. Carey, E. D. Isaac, *Magnetic domains and techniques for their observation* (Academic Press, New York, 1966).

[59] E. A. Nesbitt, J. H. Wernick, *Rare earth permanent magnets* (Academic Press, New York, 1973).

[60] T. Egami, in *Proceedings of the 17th Annual conference on magnetism and magnetic materials, No. 5* (American Institute of Physics, New York, 1972).

[61] S. Chikazumi, *Physics of magnetism* (Wiley, New York, 1964).

[62] B. D. Cullity, *Introduction to magnetic materials* (Addison-Wesley, Reading, 1972).

[63] A. H. Morrish, *The physical principles of magnetism* (Wiley, New York, 1965).

[64] L. Weil, J. Chem. Phys. 51, 715 (1954).

[65] C. P. Bean, J. Livingston, *J. App. Phys.* **30**, 1205 (1959).

[66] A. J. Leggett, *J. J. App. Phys.* **26**, supplement 26-3 (1987).

[67] M. Huth, private communication.

[68] L. Gunther, *Studies of magnetic properties of fine particles and their relevance to materials science*, J. L. Dormann, D. Fiorani, eds. (Elsevier, Amsterdam, 1992). See also S. B. Oseroff, D. Clark, S. Schultz, S. Strikman, *IEEE Trans. Mag.* **21**, 1495 (1985).

[69] L. L. Balcells, X. X. Zhang, F. Badia, J. M. Ruiz, C. Ferraté, J. Tejeda, *J. Mag. Mag. Mat.* **109**, L159-L163 (1992).

[70] E. M. Chudnovsky, *J. Mag. Mag. Mat.* **140-144**, 1821-1824 (1995).

[71] R. W. Chantrell, A. Lyberatos, M. El-Hilo, K. O'Grady, *J. App. Phys.* **76**, 6407-6412 (1994).

[72] E. Dan Dahlbert, D. K. Lottis, R. M. White, M. Matson, E. Engle, *J. App. Phys.* **76**, 6396-6400 (1994).

[73] L. Folks, R. Street, *J. App. Phys.* **76**, 6391-6395 (1994).

[74] R. Street, S. D. Brown, *J. App. Phys.* **76**, 6386-6390 (1994).